The 8th European Congress on Computational Methods in Applied Sciences and Engineering
ECCOMAS Congress 2022
5-–9 June 2022, Oslo, Norway

HIGH-ORDER, HIGH-FIDELITY SIMULATION OF UNSTEADY SHOCK-WAVE/BOUNDARY LAYER INTERACTION USING FLUX RECONSTRUCTION

N. Goffart[1,*], B. Tartinville[1], K. Puri[1], C. Hirsch[1] and S. Pirozzoli[2]

[1] Cadence Design Systems Belgium, Chaussée de la Hulpe 189, Brussels B-1170 Belgium
*ngoffart@cadence.com

[2] Department of Mechanical and Aerospace Engineering, Sapienza University of Rome, via Eudossiana 18, 00184 Rome, Italy

Key words: SWBLI, high-order, high-fidelity, flux reconstruction, shock capturing

Abstract. In this work, a high-order implicit large-eddy simulation of an oblique shock-wave/boundary layer interaction at Mach 2.3 is performed. The high-order solver is based on the flux reconstruction method, allowing an arbitrary order of accuracy. A particular attention is paid to the shock-capturing technique which consists in a combination of a Laplacian artificial viscosity with the Ducros sensor. The ability of such a solver to accurately predict the flow features is assessed on both steady and unsteady fields. In particular, the typical low-frequency motion of the reflected shock is reproduced. The shock-capturing methodology is proven to be efficient at resolving the shocks without damping the turbulence in the boundary layer. The results obtained give confidence in this solver to study in more details the shock-wave/boundary layer interaction phenomenon and future work is focused on the analysis of the oscillatory turbulent field in the interaction region.

1 INTRODUCTION

Many flows in aeronautical applications are subjected to shock-wave/boundary layer interactions (SWBLI), for example flows over aircraft wings, turbomachinery blades or in engine air intakes of supersonic aircraft. In all cases, the aerodynamic efficiency is negatively affected because of the flow separation or distortion and the low-frequency unsteadiness of the interaction is responsible for structural fatigue that can result in failure. To mitigate these effects and therefore improve current designs, more effort is to put on the understanding and the modeling of such interactions.

This work in particular is focused on oblique SWBLI. On the experimental side, it has been extensively studied by the "Institut Universitaire des Systèmes Thermiques Industriels" (IUSTI) group from Marseille, France [1, 2, 3]. On the numerical side, early works [4, 5] demonstrated the capabilities of high-fidelity simulations such as Large-Eddy Simulation (LES) and Direct Numerical Simulation (DNS) to provide an accurate prediction of the flow features. The integration time of those simulations were however too short to observe the low-frequency motion of the reflected shock. Since then, the computational power increased and many more simulations

have been performed in the literature. Among them, an investigation of the low-frequency unsteadiness and a model based on a conditional averaging analysis has been proposed [6]. A LES database has also been produced and used to assess the validity of different models describing the low-frequency motion and to study the modelling errors associated with Reynolds-Averaged Navier-Stokes (RANS) simulations [7]. Finally, a detailed analysis of the Reynolds stress budgets in the interaction region has been performed too [8].

Performing high-fidelity simulations remains costly. A remedy for this is to employ high-order numerical schemes as they allow to reach the same level of accuracy as lower-order schemes but at a reduced computing time. Recently, a unifying framework of high-order schemes based on flux reconstruction (FR) has been introduced [9]. In such schemes, a powerful shock-capturing technique is essential. The solution in each cell is indeed represented by a polynomial and sharp jumps in the flow quantities (across shocks for example) result in spurious oscillations of this representation that can lead to the divergence of the simulation.

In this context, the present work shows the results of a high-order Implicit Large-Eddy Simulation (ILES) of an oblique SWBLI. The solver makes use of a FR scheme and a Laplacian artificial viscosity method is utilized as shock-capturing technique. An adaptation of the latter is proposed to comply with the requirements of solving unsteady shock/turbulence interaction. This paper is organized as follows. The first section introduces the computational methodology, comprising the numerical schemes, the flow conditions and the simulation setup. Then, a basic validation of the flow is achieved by looking at time-averaged results and frequency analysis. Finally, the performance of the shock-capturing technique is assessed.

2 COMPUTATIONAL METHODOLOGY

2.1 Numerical schemes

The high-fidelity simulation is performed with a high-order solver based on the flux reconstruction (FR) approach [9] to calculate the spatial derivatives. This approach is a unifying framework of popular high-order methods. A particular FR scheme is defined by three characteristics: the location of the solution points, the method to compute the common values and fluxes at the cell interfaces and the type of correction functions. In the present work, Gauss points have been chosen. Roe's approach [10] is employed to compute the common advective fluxes whereas the common solutions and common diffusive fluxes are evaluated using the Local Discontinuous Galerkin approach [11] with $\beta = 0$ and $\tau = 1$ [12]. Finally, the left and right Radau polynomials are used as correction functions. This allows to recover a particular nodal Discontinuous Galerkin method. Regarding the temporal derivative, it is evaluated using a 5-stages fourth-order low-storage Runge-Kutta scheme [13].

A particular attention is given to the shock-capturing technique. It is based on a Laplacian artificial viscosity in which the shock sensor is an indicator of the modal smoothness of the solution within the cell [14]. Considering the modal expansion of a quantity q within a cell

$$q = \sum_{i=1}^{N(p)} q_i \psi_i \tag{1}$$

where $N(p)$ is the number of terms in the expansion of order p, q_i are the coefficients of the

expansion and ψ_i are the basis functions, the sensor writes

$$s_e = \log_{10}\left(\frac{(q-\hat{q}, q-\hat{q})_e}{(q,q)_e}\right) \tag{2}$$

with $\hat{q}$ the expansion in equation (1) truncated to the order $p-1$ and $(.,.)_e$ the standard inner product in the element. For smooth solutions, the expansion coefficients are expected to decrease quickly as the order of the mode increases. A high value of the sensor will then indicate the presence of a discontinuity. The artificial viscosity is finally computed based on the value of the sensor with

$$\varepsilon_e = \begin{cases} 0 & \text{if } s_e < s_0 - \kappa \\ \frac{\varepsilon_0}{2}\left(1 + \sin\frac{\pi(s_e - s_0)}{2\kappa}\right) & \text{if } s_0 - \kappa < s_e < s_0 + \kappa \\ \varepsilon_0 & \text{if } s_e > s_0 + \kappa \end{cases} \tag{3}$$

where ε_0 is given by

$$\varepsilon_0 = C_T \frac{\hat{h}}{p} \lambda_{max} \tag{4}$$

in which $\hat{h}$ is the reference grid spacing of the element, p is the polynomial order and λ_{max} is the maximum eigenvalue of the set of equations among all the solution points of the element. Equations (3) and (4) contain three user-defined parameters, namely s_0, κ and C_T which are case dependent.

When using this method as such, the sensor exhibits high values in the boundary layer due to the unsteadiness of the flow. A non-negligible amount of artificial viscosity is then applied and may cause the under-prediction of turbulence fluctuations [15]. Therefore, the Ducros sensor [16] is used in this work to further distinguish shocks from turbulence. It is indeed bounded between 0 in regions of high-vorticity and 1 around shocks. The combination is performed through an activation function

$$\varepsilon = \varepsilon_e s_D \tag{5}$$

where

$$s_D = \begin{cases} 0 & \text{if } \bar{s}_D < s_{D,0} \\ \frac{1}{2}\left(1 + \sin\left(\pi\left(\frac{\bar{s}_D - s_{D,0}}{1 - s_{D,0}} - \frac{1}{2}\right)\right)\right) & \text{if } s_{D,0} < \bar{s}_D < 1 \\ 1 & \text{if } \bar{s}_D > 1 \end{cases} \tag{6}$$

with $\bar{s}_D$ the cell-averaged Ducros sensor and $s_{D,0}$ a suitable threshold value under which the artificial viscosity is explicitly set to 0. By doing so, the shock-capturing technique will let the boundary layer untouched by the artificial viscosity.

As the original method, this provides with a cell-wise constant artificial viscosity field and it has been found to lead to spurious oscillations in the state gradients that can convect downstream and pollute the solution [17]. The field is thus C^0-smoothed following [18]. Finally, a positivity-preserving limiter is employed for additional robustness [19].

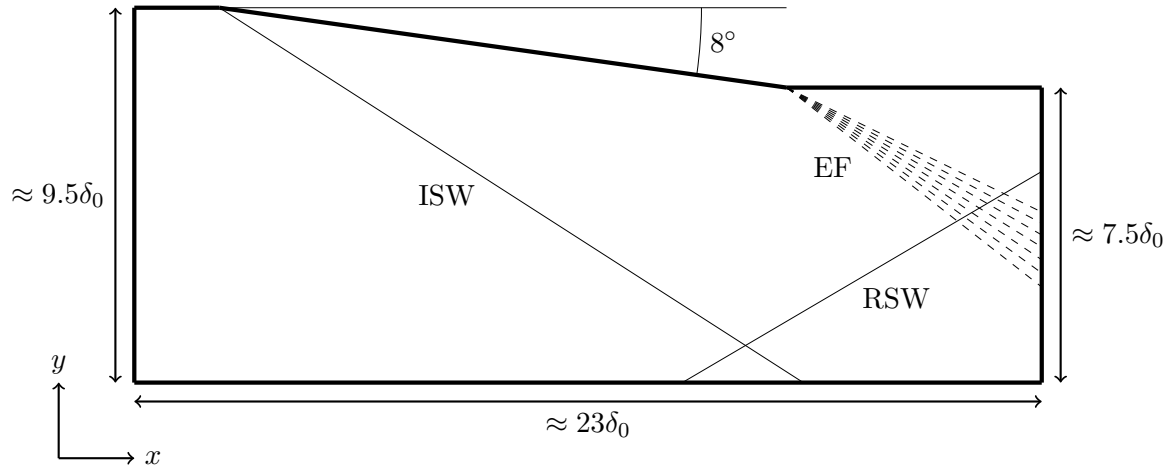

Figure 1: Side view of the computational domain with some of the main flow features: incident shock wave (ISW), reflected show wave (RSW) and expansion fan (EF).

Turbulent inflow conditions are obtained with the digital filtering technique. Instead of the original 3D filter implementation [20], the approach of a 2D filter composed of the directions tangent to the inlet plane is chosen. The filter is from inception a 2D filter and not a convolution of two 1D filters [21], making the approach valid for unstructured grids. This 2D slice is then correlated in time with the previous time step following [22]. Velocity perturbations are finally scaled with the Lund's transformation [23]. Compressible fluctuations (for temperature and density) are also introduced based on the Strong Reynolds Analogy and the hypothesis of negligible pressure fluctuations [6].

2.2 Flow conditions and simulation setup

The flow conditions correspond to an experiment led at the IUSTI in which an oblique shock-wave is generated with a flat plate inclined by 8° in a Mach 2.3 flow and impinges on the turbulent boundary layer developed on the floor of the wind tunnel [3]. Upstream of the interaction, the boundary layer thickness is 11 mm and the Reynolds number based on the incompressible momentum thickness Re_{θ_i} is around 6900. The friction coefficient C_f is 0.002 and the total temperature is 300 K. These conditions are matched in the present work.

A side view of the computational domain is shown in figure 1 with some of the main flow features. The incident shock is generated by the inclination of the top boundary. The streamwise extent of the domain is $\approx 23\delta_0$, with the inlet located $\approx 17\delta_0$ upstream of the inviscid impingement point of the incident shock. This allows the upstream turbulence to develop properly before reaching the interaction region, the adaptation distance being typically around 10 to $20\delta_0$ [21]. In the spanwise direction, the domain length is $5\delta_0$ which is sufficiently large to ensure that the turbulence structures are decorrelated. Finally, in the wall-normal direction, the domain height is approximately $9.5\delta_0$ at the inlet and $7.5\delta_0$ at the outlet.

The mesh is entirely composed of hexahedra. The number of cells is 256 x 97 x 76 in the streamwise, wall-normal and spanwise directions. The simulation is performed at polynomial order 3, leading to a total number of solution points of around 121 millions. A constant grid

spacing is used in the x and z directions giving in wall units $\Delta_x^+ \approx 16.5$ and $\Delta_z^+ \approx 12$. In the wall-normal direction, the boundary layer comprises exactly 25 cells (100 solution points at polynomial order 3) which are stretched according to a hyperbolic tangent law. The first cell height is imposed such that the first solution point lies below $y^+ = 1$. Outside the boundary layer, the cell height is kept practically constant and equal to the grid spacing in the streamwise direction, leading to $\Delta_y^+ \approx 16.5$. Note that the grid spacing is evaluated here with respect to the solution points.

Regarding the boundary conditions, the inlet is fully supersonic with prescribed velocity components, static temperature and static pressure profiles. These come from a precursor ILES of a turbulent boundary layer in the same flow conditions. To configure the digital filter, turbulence length scales in the streamwise I_x and spanwise I_z directions have been set constant and respectively equal to $0.5\delta_0$ and $0.2\delta_0$. I_y varies in the wall-normal direction such that the number of flux points constituting the filter is practically constant and around 350. Moreover, it matches I_z at the edge of the boundary layer. Reynolds stresses profiles (obtained from the same precursor simulation) are imposed to scale the filtered perturbations.

The outlet boundary is supersonic but with static pressure imposed in the subsonic part of the boundary layer. The value is taken from a separate RANS simulation of the interaction, at the first supersonic point in the outlet boundary layer. The top boundary is divided into a slip wall for the shock generator and two external boundaries with Riemann invariants. The bottom wall is no-slip adiabatic and periodic boundary conditions are prescribed in the spanwise direction.

Finally, the simulation is performed at polynomial order 3, making the FR method employed fourth-order accurate. The explicit time step is 2.5×10^{-8}s, leading to a CFL number ≈ 2.5. The parameters of the shock-capturing technique are $s_0 = -4.5$, $\kappa = 0.5$, $C_T = 0.03$ and $s_{D,0} = 0.2$. Density is used as the sensor variable.

3 RESULTS

3.1 Basic flow validation

A first insight into the flow field is given in figure 2 displaying an instantaneous view of the density gradient at mid-span. The incident shock and its reflection as an expansion fan on the sonic line can easily be recognized. As expected, the reflected shock-wave stands slightly upstream of its inviscid location. Turbulence structures are clearly highlighted in the upstream boundary layer and are largely influenced by the interaction. The weak reattachment shock-wave, turning back the flow parallel to the wall after the interaction, can also be discerned.

The time- and span-averaged boundary layer profile upstream of the interaction is shown in figure 3. Compared with the ILES data from [8], the curves are practically on top of each others even tough the mesh here is twice less refined in the spanwise direction. With respect to PIV measurements [3], a slight offset in the logarithmic region (with $\kappa = 0.41$ and $C = 5.1$) can be observed and is due to an under-prediction of the friction velocity u_τ by 2.5%. This under-prediction originates from the grid resolution. Moving to polynomial order 4 showed indeed an improvement but at a much higher computational cost.

Figure 3 (*right*) presents the velocity perturbations profiles and compare them to the available PIV data and other simulations using digital filtering [6, 8]. In comparison to PIV, the peak

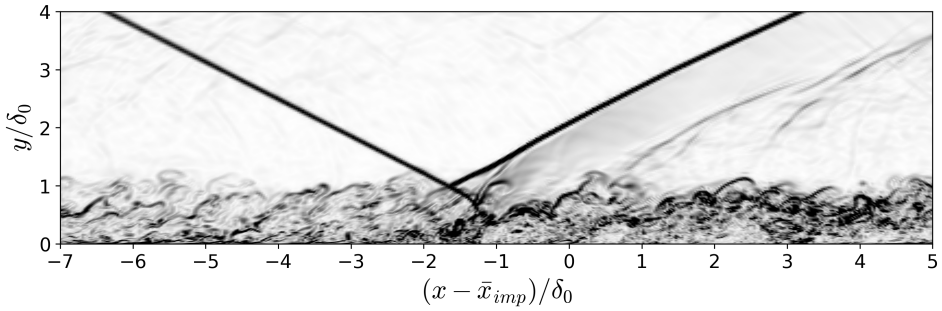

Figure 2: Side view of instantaneous density gradient.

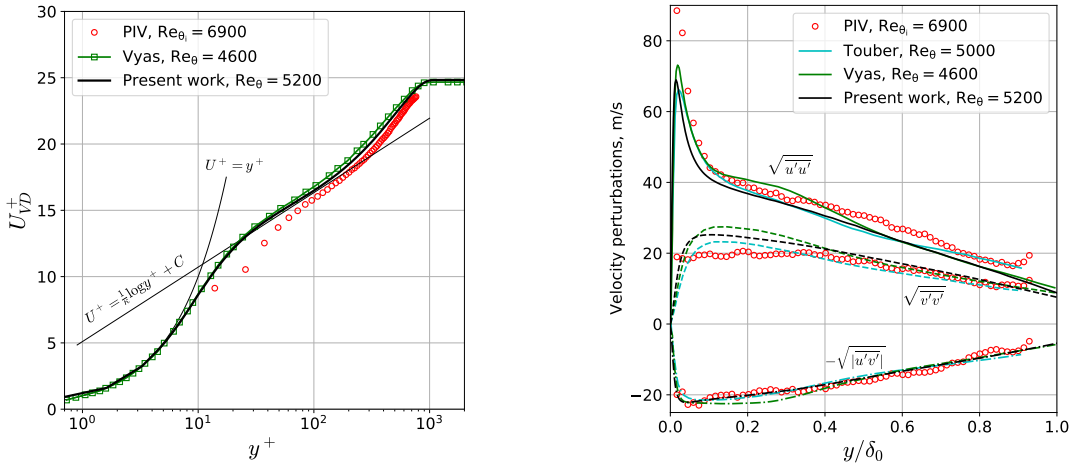

Figure 3: Streamwise velocity (*left*) and stresses profiles (*right*) at $(x - \bar{x}_{imp})/L$ = -1.66.

of u' is under-predicted and an overshoot is found for v' near the wall. These are however common features among the other simulations results and the error might come from the near-wall measurements. The lower level of streamwise velocity perturbations in the outer layer can be attributed to the recovery effects of the digital filtering approach [6]. Despite these differences, the agreement remains very good.

The streamwise evolution of friction coefficient is displayed in figure 4 (*left*) and compared with two other ILES at similar Reynolds numbers [7, 8]. Upstream of the interaction, the friction coefficient is slightly decreasing, as expected for a developed turbulent boundary layer. Together with the boundary layer profiles shown in figure 3, this is comforting the idea that the inlet is located far enough upstream of the interaction region to let the boundary layer retrieve its main features but also that the digital filtering is correctly configured. Within the interaction, two lobes can be observed, the first one indicating an incipient separation and the second one showing a clear separated region. This is somehow different from the other results, which predict two separated regions. Moreover, the effect of the adverse pressure gradient is felt more upstream in the present work. The exact origin of this change in the topology of the recirculation bubble is not known. A preliminary run also resulted in two clear separated regions. However, the

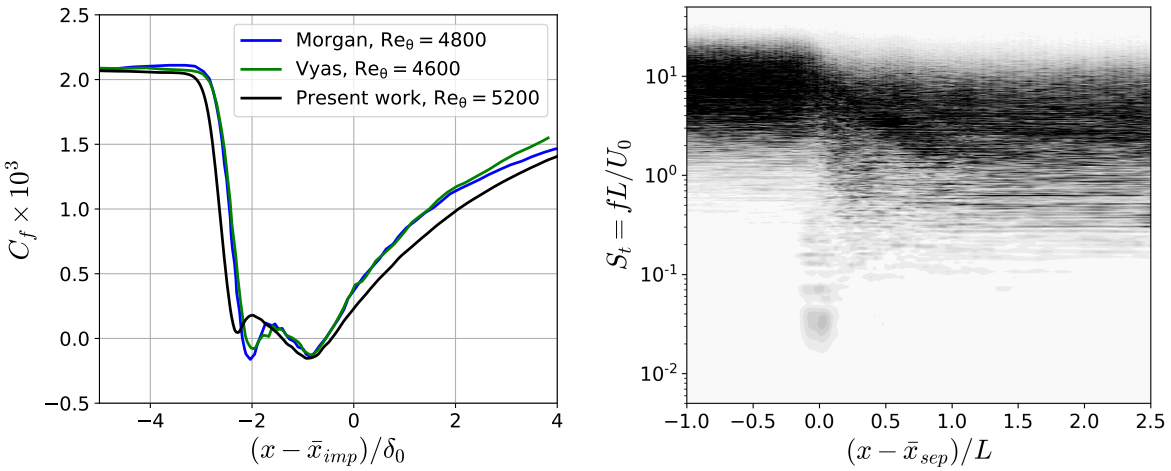

Figure 4: Streamwise evolution of friction coefficient (*left*) and weighted pre-multiplied PSD map of pressure fluctuations signals (*right*).

upstream boundary layer was not as well established as the one reported here. The friction coefficient was still slightly increasing before the interaction, for instance as in the results of [7]. Moreover, a slight amount of artificial viscosity was remaining in the interaction region because a linear activation function for the Ducros sensor was used. It is therefore believed that the friction coefficient is very sensitive to the upstream boundary layer and/or the (artificial) dissipation of the scheme. It is also interesting to note that, even though the separation length is consequently slightly larger compared to the other simulation results, the length of interaction L is similar, with $3.01\delta_0$ in the present work against $3.02\delta_0$ [7] and $2.96\delta_0$ [8].

Figure 4 (*right*) shows the weighted pre-multiplied power spectral density (PSD) map of wall pressure fluctuations. The pressure data has been acquired at a sampling rate of 50 MHz for a reduced time covering $\approx 1000\delta_0/U_0$. As expected, an energetic broadband low-frequency region can be observed near the mean separation point. The Strouhal number based on the interaction length is about two orders of magnitude lower than the characteristic Strouhal number of the incoming boundary layer. The peak S_t is ≈ 0.03, whereas experimental values lie between 0.025 and 0.04 for shock generator angles from 9.5° to 7° [1]. The ridge constituted by the upstream boundary layer is slightly shifted to lower frequencies after the interaction since the boundary layer thickness has increased. As a consequence, larger turbulence structures with larger time scales appear.

3.2 Shock-capturing technique performance

The shock-capturing technique is of prime importance in shock/turbulence interaction and its performance is assessed hereunder. To illustrate the principle of the technique employed here in more details, figure 5 shows side views of the averaged shock sensor, Ducros sensor and artificial viscosity fields. Note that the artificial viscosity is normalised by the local kinematic viscosity to compare the magnitude of the different viscous effects. The original method applies artificial viscosity for any cell in which the shock sensor s_e is higher than $s_0 - \kappa$. It can be

noticed from the left figure that it corresponds to the shocks but also the boundary layer. The latter is problematic since it will damp the turbulence. The Ducros sensor is proposed as an additional step to discriminate the boundary layer and the central figure justifies this choice. The artificial viscosity is indeed explicitly set to 0 for every cell below the threshold value $s_{D,0}$. The resulting artificial viscosity field is therefore concentrated around the shocks only as it can be observed on the right figure.

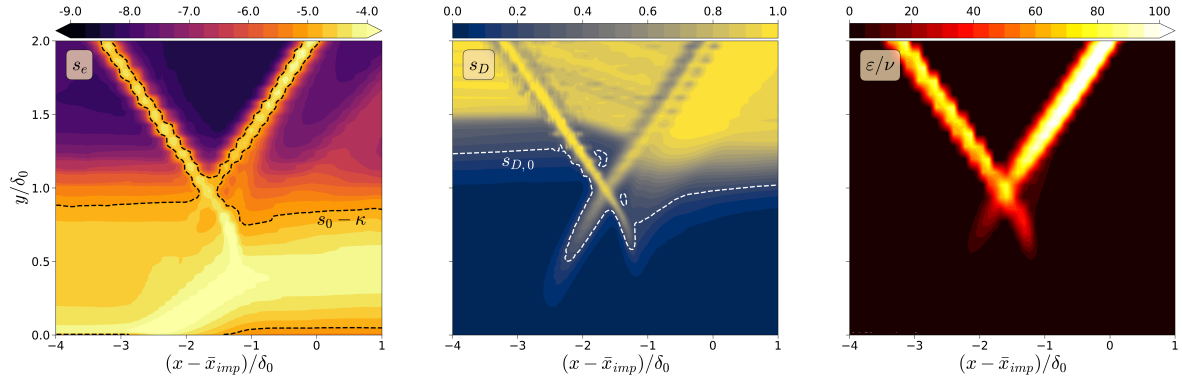

Figure 5: Side views of the averaged shock sensor (*left*), Ducros sensor (*center*) and artificial viscosity (*right*).

To further prove that the boundary layer is effectively exempted from artificial viscosity, figure 6 shows the streamwise evolution of s_e, s_D and ε/ν at $y/\delta_0 = 0.2$. As stated previously, the shock sensor is high enough at all streamwise locations to trigger the artificial viscosity but none should be applied since the Ducros sensor is far below its threshold value. This is indeed the case for the vast majority of streamwise locations. Nevertheless, tiny amounts can still be observed and correspond to the prints left by the shocks penetrating the boundary layer. These prints might originate from instantaneous events during which no significant vortical structure is passing through the shocks, leading to a higher value of the Ducros sensor. As the order of magnitude of these remaining amounts is several times lower than what is needed to capture the shocks, these events are rare. This would also explain why practically nothing can be detected near the incident shock. Turbulence is indeed promoted in the interaction region and it makes the occurrence even more uncommon. Considering the rarity of such events, they are believed to have no influence on the interaction.

Finally, it should not be forgotten that the first requirement of a shock-capturing technique is to properly resolve the sharp jump in the flow quantities imposed by the shocks and avoid any spurious oscillation due to the high-order representation of the solution within the cell. Figure 7 depicts the streamwise evolution of static pressure in the potential flow and it can be observed that both shocks are correctly smoothened.

4 CONCLUSIONS

An implicit large-eddy simulation of an oblique shock-wave/boundary layer interaction has been performed. The solver uses a high-order scheme derived from the flux reconstruction

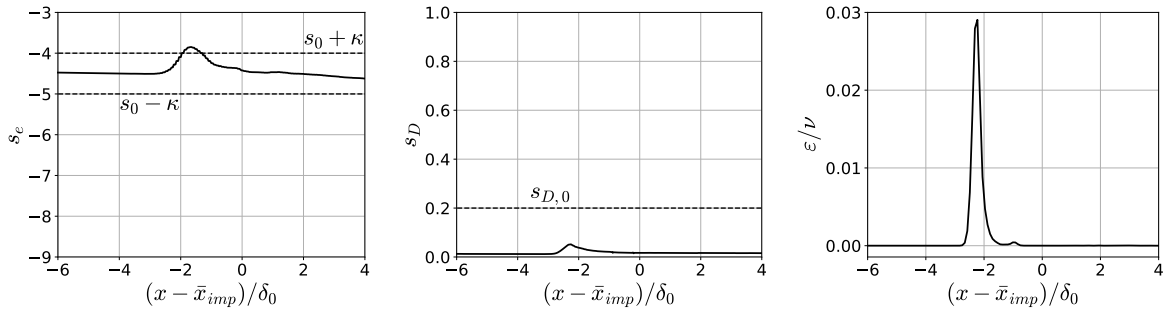

Figure 6: Streamwise evolution of the averaged shock sensor (*left*), Ducros sensor (*center*) and artificial viscosity (*right*) at $y/\delta_0 = 0.2$.

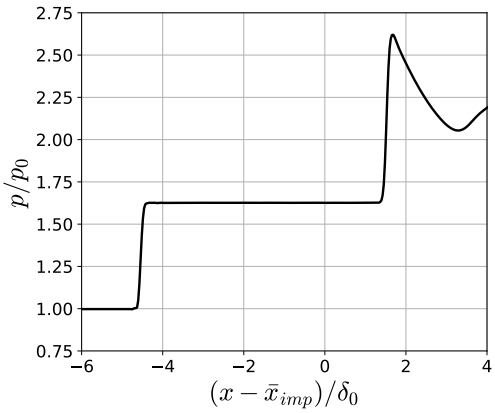

Figure 7: Averaged static pressure evolution at $y/\delta_0 = 3.0$.

approach. The shock-capturing technique combines an existing method of Laplacian artificial viscosity with the Ducros sensor to avoid undesired artificial viscosity in the boundary layer, which would damp the turbulence.

Basic flow features have been reproduced and compared to experimental and other simulations results in the literature. The friction coefficient is different from what has been shown in the past but the simulation setup is of better quality here. The low-frequency motion of the reflected shock, typical of SWBLI, exhibits a characteristic Strouhal number two orders of magnitude lower than the turbulence of the upstream boundary layer.

The shock-capturing technique has been proven to be efficient at distinguishing the shock system from the boundary layer and therefore the artificial viscosity is concentrated only around shocks. A tiny amount is still perceptible in the interaction region due to the penetration of the shocks but is negligible. The set of parameters employed is adequate as no spurious oscillations in the flow quantities can be observed across the shocks.

These results give confidence in the solver to study shock-wave/boundary layer interactions. Forthcoming analysis will be based on conditional averaging and will aim at studying how the oscillatory shock motion is affecting the turbulent stresses.

ACKNOWLEDGEMENTS

This project has received funding from the European Union's Horizon 2020 research and innovation programme under the grant agreement MSCA-ITN-ETN TEAMAero No 860909.

REFERENCES

[1] Dussauge, J. P., Dupont, P., & Debiève, J. F. (2006). Unsteadiness in Shock Wave Boundary Layer Interactions with Separation. *Aerospace Science and Technology*, *10*(2), 85-91. https://doi.org/10.1016/j.ast.2005.09.006

[2] Dupont, P., Haddad, C., & Debieve, J. F. (2006). Space and Time Organization in a Shock-Induced Separated Boundary Layer. *Journal of Fluid Mechanics*, *559*, 255-277. https://doi.org/10.1017/S0022112006000267

[3] Dupont, P., Piponniau, S., Sidorenko, A., & Debiève, J. F. (2008). Investigation by Particle Image Velocimetry Measurements of Oblique Shock Reflection with Separation. *AIAA Journal*, *46*(6), 1365-1370. https://doi.org/10.2514/1.30154

[4] Garnier, E., Sagaut, P., & Deville, M. (2002). Large Eddy Simulation of Shock/Boundary-Layer Interaction. *AIAA Journal*, *40*(10), 1935-1944. https://doi.org/10.2514/2.1552

[5] Pirozzoli, S., & Grasso, F. (2006). Direct Numerical Simulation of Impinging Shock Wave/Turbulent Boundary Layer Interaction at M = 2.25. *Physics of fluids*, *18*(6), 065113. https://doi.org/10.1063/1.2216989

[6] Touber, E. (2010). *Unsteadiness in Shock-Wave/Boundary Layer Interactions* (Doctoral dissertation, University of Southampton).

[7] Morgan, B., Duraisamy, K., Nguyen, N., Kawai, S., & Lele, S. K. (2013). Flow Physics and RANS Modelling of Oblique Shock/Turbulent Boundary Layer Interaction. *Journal of Fluid Mechanics*, *729*, 231-284. https://doi:10.1017/jfm.2013.301

[8] Vyas, M. A., Yoder, D. A., & Gaitonde, D. V. (2019). Reynolds-Stress Budgets in an Impinging Shock-Wave/Boundary-Layer Interaction. *AIAA Journal*, *57*(11), 4698-4714. https://doi.org/10.2514/1.J058487

[9] Huynh, H. T. (2007). A Flux Reconstruction Approach to High-Order Schemes Including Discontinuous Galerkin Methods. *In 18th AIAA Computational Fluid Dynamics Conference* (p. 4079). https://doi.org/10.2514/6.2007-4079

[10] Roe, P. L. (1981). Approximate Riemann Solvers, Parameter Vectors, and Difference Schemes. *Journal of Computational Physics*, *43*(2), 357-372. https://doi.org/10.1016/0021-9991(81)90128-5

[11] Cockburn, B., & Shu, C. W. (1998). The Local Discontinuous Galerkin Method for Time-Dependent Convection-Diffusion Systems. *SIAM Journal on Numerical Analysis*, *35*(6), 2440-2463. https://doi.org/10.1137/S0036142997316712

[12] Castonguay, P., Vincent, P. E., & Jameson, A. (2012). A New Class of High-Order Energy Stable Flux Reconstruction Schemes for Triangular Elements. *Journal of Scientific Computing*, *51*(1), 224-256. https://doi.org/10.1007/s10915-011-9505-3

[13] Carpenter, M. H., & Kennedy, C. A. (1994). Fourth-Order 2N-storage Runge-Kutta Schemes (No. NASA-TM-109112).

[14] Persson, P. O., & Peraire, J. (2006). Sub-Cell Shock Capturing for Discontinuous Galerkin Methods. *In 44th AIAA Aerospace Sciences Meeting and Exhibit* (p. 112). https://doi.org/10.2514/6.2006-112.

[15] Mani, A., Larsson, J., & Moin, P. (2009). Suitability of Artificial Bulk Viscosity for Large-Eddy Simulation of Turbulent Flows with Shocks. *Journal of Computational Physics*, *228*(19), 7368-7374. https://doi.org/10.1016/j.jcp.2009.06.040

[16] Ducros, F., Ferrand, V., Nicoud, F., Weber, C., Darracq, D., Gacherieu, C., & Poinsot, T. (1999). Large-Eddy Simulation of the Shock/Turbulence Interaction. *Journal of Computational Physics*, *152*(2), 517-549. https://doi.org/10.1006/jcph.1999.6238

[17] Barter, G. E., & Darmofal, D. L. (2010). Shock Capturing with PDE-based Artificial Viscosity for DGFEM: Part I. Formulation. *Journal of Computational Physics*, *229*(5), 1810-1827. https://doi.org/10.1016/j.jcp.2009.11.010

[18] Persson, P. O. (2013). Shock Capturing for High-Order Discontinuous Galerkin Simulation of Transient Flow Problems. *In 21st AIAA Computational Fluid Dynamics Conference* (p. 3061). https://doi.org/10.2514/6.2013-3061

[19] Wang, C., Zhang, X., Shu, C. W., & Ning, J. (2012). Robust High Order Discontinuous Galerkin Schemes for Two-Dimensional Gaseous Detonations. *Journal of Computational Physics*, *231*(2), 653-665. https://doi.org/10.1016/j.jcp.2011.10.002

[20] Klein, M., Sadiki, A., & Janicka, J. (2003). A Digital Filter Based Generation of Inflow Data for Spatially Developing Direct Numerical or Large Eddy Simulations. *Journal of Computational Physics*, *186*(2), 652-665. https://doi.org/10.1016/S0021-9991(03)00090-1

[21] Adler, M. C., Gonzalez, D. R., Stack, C. M., & Gaitonde, D. V. (2018). Synthetic Generation of Equilibrium Boundary Layer Turbulence from Modeled Statistics. *Computers & Fluids*, *165*, 127-143. https://doi.org/10.1016/j.compfluid.2018.01.003

[22] Xie, Z. T., & Castro, I. P. (2008). Efficient Generation of Inflow Conditions for Large Eddy Simulation of Street-Scale Flows. *Flow, Turbulence and Combustion*, *81*(3), 449-470. https://doi.org/10.1007/s10494-008-9151-5

[23] Lund, T. S., Wu, X., & Squires, K. D. (1998). Generation of Turbulent Inflow Data for Spatially-Developing Boundary Layer Simulations. *Journal of Computational Physics*, *140*(2), 233-258. https://doi.org/10.1006/jcph.1998.5882